Experimental identification and physical interpretations of 2D tensor magnetic properties of a Grain Oriented Electrical Steel magnetized between the rolling and the transverse directions

Olivier Maloberti, Préscillia Dupont, Théo Etifier, Elias Salloum, Pascal Dassonvalle, Jérôme Fortin, Stéphane Panier

Experimental identification and physical interpretations of 2D tensor magnetic properties of a Grain Oriented Electrical Steel magnetized between the rolling and the transverse directions

O. Maloberti[1,2,*], P. Dupont[2,3], T. Etifier[1,2], E. Salloum[1] ,P. Dassonvalle[1,4], J. Fortin[1], S. Panier[2]

[1]SYMADE-UNILASALLE Amiens, 14 quai de la Somme, Amiens, 80080, France
[2]Labortoire LTI, IUT d'Amiens, Avenue des Facultés – Le Bailly, Amiens, 80025, France
[3]JEUMONT Electric, 367 rue de l'Industrie, Jeumont, 59460, France
[4]Laboratoire MIS, UPJV, 14 quai de la Somme, Amiens, 80080, France

This work investigates a 2D vector field behavioral model to describe the anisotropic magnetic permeability and losses in Grain Oriented Electrical Steels (GOES) within quasi-static and magneto-harmonic working conditions. The model includes the an-hysteretic magnetic field driven by the total anisotropy, the coercive force responsible for the quasi-static hysteresis losses and the dynamic damping eddy field responsible for the extra losses. Each field contribution requires the definition of a tensor property whose diagonal and non diagonal coupling components are experimentally identified as a function of the flux density magnitude B and its angle θ with the Rolling direction (*RD*). The static behavior is identified at low frequency and the dynamic one takes the frequency dependent field diffusion into account. Diagonalization tools reveal main characteristic magnetic axis for the separate properties with deflections at the macroscale.

***Index Terms* — grain oriented electrical steels, losses, magnetic structure, permeability, tensor properties, 2D vector magnetic field.**

I. Introduction – Context and State of the Art

Iron loss and dynamic hysteresis models either 1-D scalar [1, 4] or 2-D vectorial [6] are based on a separation principle between the classical losses and the microscopic ones due to reversal mechanisms. Combining the local behavior to the field diffusion equations has been proposed up to now for scalar models [7]. Developing both vector hysteresis models [8] and loss models [9] in 2D is still a subject of research to compute a magnetic flux that makes an angle with *RD* in electrical steels used for transformers, inductors and machines (Fig. 1).

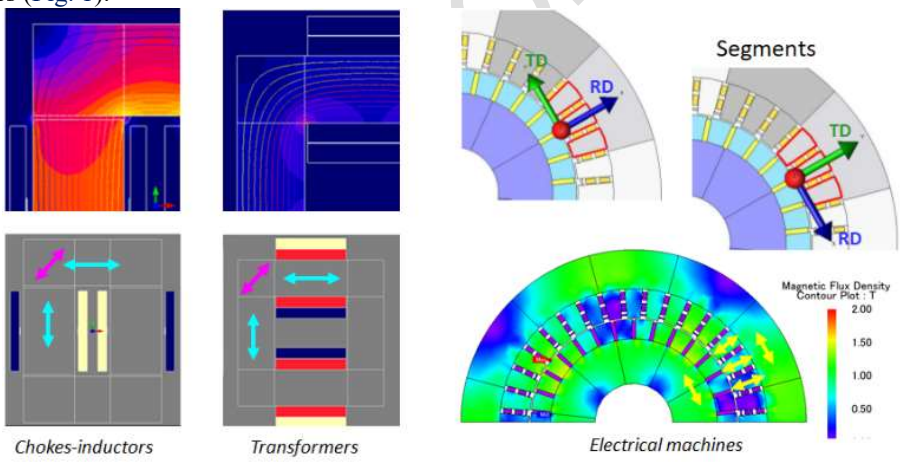

Fig. 1: Application of proposed methodology (transformers, chokes, machines).

II. The Vector Model - Tensor Magnetic Properties

A. General behavioral model

Inspiring from [1, 4, 6] and following the reference [8], we work with a complex magneto-harmonic behavior between the magnetic field $\boldsymbol{H}$ and the flux density $\boldsymbol{B}$, resulting from the minimization of the total energy state including the losses as a function of $\boldsymbol{B}$, involving three contributions (1): the static an-hysteretic magnetic field $\boldsymbol{H}_M$ at equilibrium, the quasi static coercive field $\boldsymbol{H}_h$ responsible for the quasi-static hysteresis losses and the dynamic damping magnetic field $\boldsymbol{H}_d$ due to microscopic eddy currents (see Fig. 2).

$$\boldsymbol{H}(B,) = \boldsymbol{H}_M(\boldsymbol{B}) + \boldsymbol{H}_h(\boldsymbol{B}) + \boldsymbol{H}_d(\boldsymbol{B},\omega) \quad (1)$$

This quasi-linear law within time harmonics at frequency f and angle velocity $\omega = 2\pi f$ is only able to relate the magnetic field and the flux density but not yet the hysteresis loops. Therefore, it is mainly used to estimate the magnitude permeability and losses given by each cycle slope and area.

*Corresponding author: olivie.maloberti@gmail.com

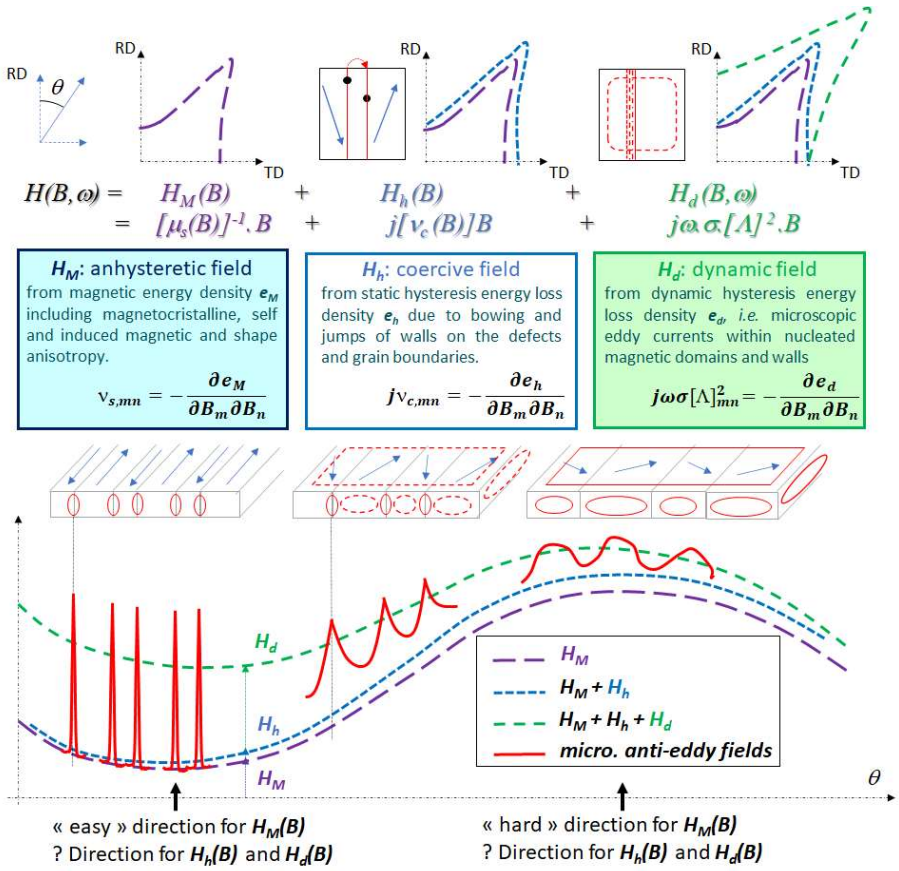

Fig. 2: Physical principles of the 2D vector field model for magnetic materials.

1) The static an-hysteretic field

This static an-hysteretic field contribution $\boldsymbol{H}_M$ is non dissipative and closely related to the magnetic anisotropy of the material (magneto-crystalline anisotropy, metallographic shape anisotropy, stress induced anisotropy). $[\nu_s] = [\mu_s]^{-1}$ is defined as the static internal magnetic reluctivity and it is a tensor derived from the non-dissipative magnetic energy density e_M, responsible for the major part of reactive power (3).

$$\boldsymbol{H}_M(\boldsymbol{B}) = [\nu_s(\boldsymbol{B})]\boldsymbol{B} = [\mu_s(\boldsymbol{B})]^{-1}\boldsymbol{B} \tag{2}$$

$$\nu_{s,mn} = -\frac{\partial e_M}{\partial B_m \partial B_n} \tag{3}$$

2) The quasi-static coercive field

The quasi-static coercive field $\boldsymbol{H}_h$ is dissipative and corresponds to microscopic anti-eddy fields mainly due to jumps of walls at defects and grains boundaries. The tensor $[\nu_c] = [\mu_c]^{-1}$ is defined as the coercive reluctivity, closely linked to non reversibility of magnetization at very low frequency [3] (4) ($j=exp(i\pi/2)$). $[\nu_c]$ is derived from the static hysteresis energy loss density e_h (5) responsible for the static hysteresis active power loss density $p_{hv} = real(\frac{1}{2}j\omega e_h)$:

$$\boldsymbol{H}_h(\boldsymbol{B}) = j[\nu_c(\boldsymbol{B})]\boldsymbol{B} \tag{4}$$

$$j\nu_{c,mn} = -\frac{\partial e_h}{\partial B_m \partial B_n} \tag{5}$$

3) The dynamic damping eddy field

At the mesoscopic scale, the magnetization reversal processes induce microscopic eddy currents that generate the extra damping magnetic field $\boldsymbol{H}_d$. It can be expressed as a function of the electrical conductivity σ, the angle velocity ω and a structural dynamic magnetization property called $[\Lambda]$ (6). $[\Lambda]$ represents and lumps the magnetic domains and walls properties [8] averaged among various orientations $\vec{\theta}_w$ with the help of the product tensor $[\varpi(\theta_w)] = \overrightarrow{\theta_w} \otimes \overrightarrow{\theta_w} = \overrightarrow{\theta_w} \cdot \overrightarrow{\theta_w}^t$) (8). The generalization proposal consists in deriving the excess energy loss density e_d (7) due to microscopic eddy currents within nucleated magnetic domains and walls and responsible for the dynamic hysteresis active power loss density [8].

$$\boldsymbol{H}_d(\boldsymbol{B}) = j\omega\sigma[\Lambda(\boldsymbol{B},\omega)]^2\boldsymbol{B} \tag{6}$$

$$j\omega\sigma[\Lambda]^2{}_{mn} = --\frac{\partial e_d}{\partial B_m \partial B_n} \tag{7}$$

$$[\Lambda(\boldsymbol{B},\omega)]^2 = \langle \frac{1}{2\sigma J_s n_w \eta_w S_w}[\varpi(\theta_w)] + S_{DMR,w}([1]-[\varpi(\theta_w)]) \rangle_{\vec{\theta}_w} \tag{8}$$

S_w is the walls surface, η_w the walls mobility and n_w the walls density [2] stand for the **D**omain **W**alls **D**isplacement (**DWD**). $S_{DMR,w}$ is the domains surface polarizability [5] and stands for the **D**omain **M**agnetization **R**otation (**DMR**) mechanism.

B. Tensor magnetic properties

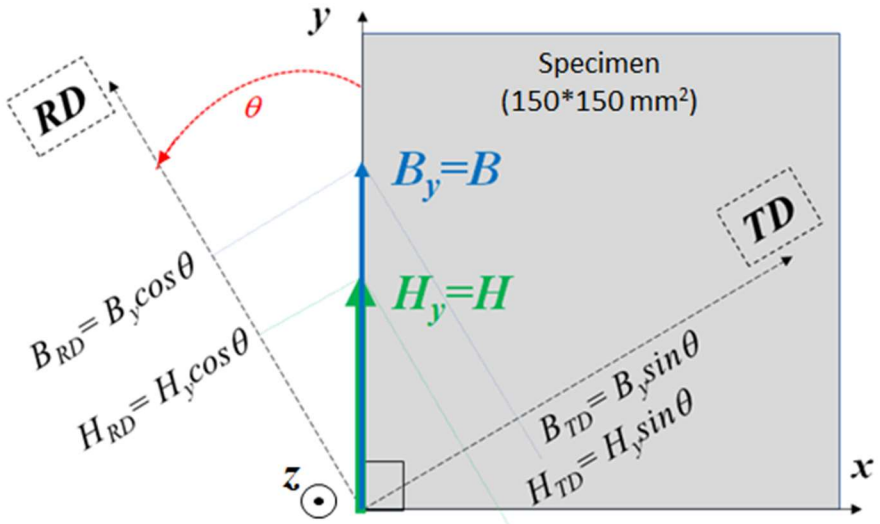

Fig. 3. Description of (*x,y*) and (*TD,RD*) reference frames. Definition of angle θ between the flux direction *y* and the rolling direction *RD*.

The most natural reference frame called (*TD,RD*) for GOES contains the two perpendicular directions known as the Transverse Direction (*TD*) and the Rolling direction (*RD*).

Given a magnetic flux density *B* oriented in the direction *y*, forming an angle θ with the rolling direction *RD*, the *TD* and *RD* components of *B* can be deduced as follows (Fig. 3):

$$B_{TD} = B\sin\theta \text{ and } B_{RD} = B\cos\theta \tag{9a}$$

$$B = \sqrt{B_{TD}^2 + B_{RD}^2} \tag{9b}$$

$$[T]_{(TD,RD)-(x,y)} = \begin{bmatrix} \cos\theta & -\sin\theta \\ \sin\theta & \cos\theta \end{bmatrix} \tag{9c}$$

The (*x,y*) reference frame being the frame related to the magnetic measurements, the normalized change of frame transfer matrix from (*x,y*) to (*TD,RD*) is given by (9c). It will be shown in the following that tensor properties are not necessarily diagonal in the (*TD,RD*) reference frame, meaning that $\boldsymbol{H}_{TD}$ does not depend only on $\boldsymbol{B}_{TD}$ but $\boldsymbol{H}_{TD}(\boldsymbol{B}_{TD},\boldsymbol{B}_{RD})$. $\boldsymbol{H}_{RD}$ does not depend only on $\boldsymbol{B}_{RD}$ but $\boldsymbol{H}_{RD}(\boldsymbol{B}_{TD},\boldsymbol{B}_{RD})$. The important issue addressed in this work consists in finding the (***XH***,***YH***) main reference frame in which tensor properties will be diagonal (see Fig. 4). These magnetic axis may be different for $[\mu_s]$, $[\nu_c]$ and $[\Lambda]$ respectively. This goal requires to identify first the non-diagonal coupling *TD-RD* components.

$\boldsymbol{\Phi}$	Direction of magnetic flux
$\boldsymbol{XH_M}$ $\boldsymbol{YH_M}$	eigenvectors for quasi-static anhysteretic field $\boldsymbol{H_M}$
$\boldsymbol{XH_h}$ $\boldsymbol{YH_h}$	eigenvectors for static hysteretis coercive field $\boldsymbol{H_h}$
$\boldsymbol{XH_d}$ $\boldsymbol{YH_d}$	eigenvectors for dynamic magnetization field $\boldsymbol{H_d}$

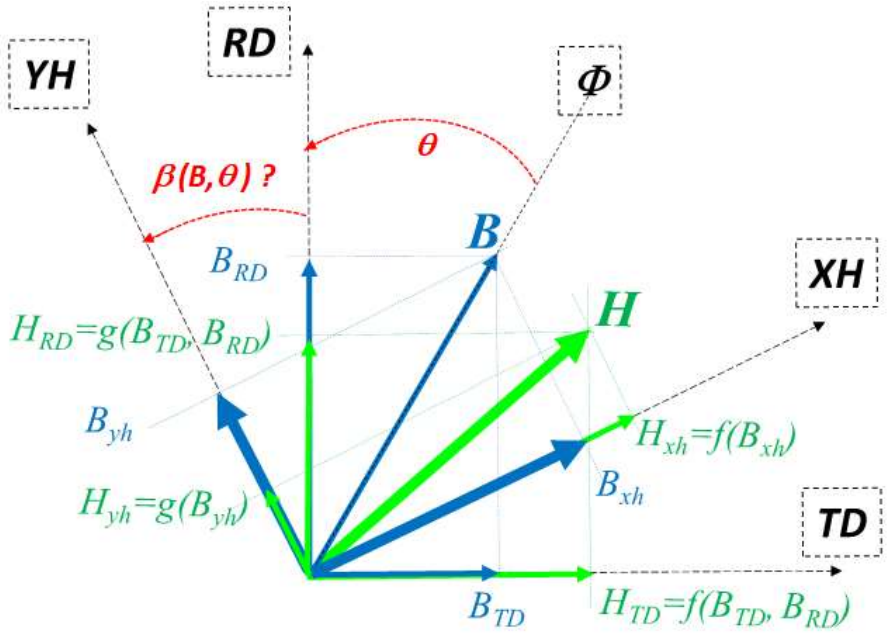

Fig. 4: Definition of reference frames for matrix diagonalization.

1) An-hysteretic quasi-static internal permeability

The an-hysteretic field $\boldsymbol{H}_M$ involves the static internal magnetic permeability $[\mu_s] = [\nu_s]^{-1} = \mu_0[\mu_{sr}]$, a symmetrical tensor. We consider the non-linear diagonal components $\mu_{sr,TD} = \mu_{sr,TD-TD}$ and $\mu_{sr,RD} = \mu_{sr,RD-RD}$ of $[\mu_{sr}]$ as a function of B_{TD} and B_{RD} respectively. Any cross dependence between *TD* and *RD* are included in the non-diagonal $\mu_{sr,TRD} = \mu_{sr,TD-RD}$ components .The vector field dependences of the latter must be identified to find the eigenvectors $\boldsymbol{XH_M}$ and $\boldsymbol{YH_M}$ depending on *B* and angle θ. It gives information on the total anisotropy energy density $e_M(\theta)$ and its main macroscopic magnetic axis.

$$[\mu_s] = \mu_0 \begin{bmatrix} \mu_{sr,TD}(B_{TD}) & \mu_{sr,TRD}(B,\theta) \\ \mu_{sr,TRD}(B,\theta) & \mu_{sr,RD}(B_{RD}) \end{bmatrix}_{(TD,RD)} \tag{10}$$

2) Static coercive reluctivity and static hysteresis losses

The static coercive field $\boldsymbol{H}_h$ involves the coercive magnetic permeability $[\mu_c]$ or its inverse, the reluctivity $[\nu_c] = [\mu_c]^{-1}$,

$$[\mu_c] = \mu_0 \begin{bmatrix} \mu_{cr,TD}(B_{TD}) & \mu_{cr,TRD}(B,\theta) \\ \mu^*_{cr,TRD}(B,\theta) & \mu_{cr,RD}(B_{RD}) \end{bmatrix}_{(TD,RD)} \tag{11a}$$

$$p_{hm} = \frac{p_{hv}}{\gamma} = real(\frac{1}{2\gamma}\boldsymbol{H}_h \cdot (j\omega\boldsymbol{B})^*) = \frac{1}{2\gamma}[\nu_c]\omega\boldsymbol{B}\cdot\boldsymbol{B}^* \tag{11b}$$

This field is responsible for the static hysteresis losses given by equation (11b) (γ being the mass density). The diagonal *RD* component of $[\nu_c]$ is related to the hysteresis loss coefficient K_h of Bertotti [1, 4] in case of 1-directional flux ($\pi\,\nu_{c,RD} = K_h$).
We consider the non-linear diagonal components $\mu_{cr,TD} = \mu_{cr,TD-TD}$ and $\mu_{cr,RD} = \mu_{cr,RD-RD}$ of $[\mu_{cr}]$ as a function of the induction components B_{TD} and B_{RD} respectively. Any cross dependence between *TD* and *RD* are included in the non-diagonal $\mu_{cr,TRD} = \mu_{cr,TD-RD}$ components .The vector field dependences of the latter must be identified to find the eigenvectors $\boldsymbol{XH_h}$ and $\boldsymbol{YH_h}$ depending on *B* and angle θ. It gives information on the static hysteresis energy loss density $e_h(\theta)$, linked to grains shape and boundaries or dislocations directions.

3) Dynamic and structural magnetization property

The dynamic field $\boldsymbol{H}_d$ involves the magnetic structure represented by $[\Lambda]$, an Hermitian tensor whose components Λ_{ij} are equivalent to a local excess loss coefficient relative to $j\omega B_i$ and $j\omega B_j$. In ordered to fit the measurements, the diagonal components $\Lambda_{TD} = \Lambda_{TD-TD}$ and $\Lambda_{RD} = \Lambda_{RD-RD}$ of $[\Lambda]$ must be considered non-linear and dependent on both components (B_{TD}, B_{RD}) and the frequency *f*. The vector field dependences of non-diagonal $\Lambda_{TRD} = \Lambda_{TD-RD}$ can also be identified to find the eigenvectors $\boldsymbol{XH_d}$ and $\boldsymbol{YH_d}$ depending on *B* and angle θ(12). It gives information on the excess energy loss density $e_d(\theta)$ linked to activated magnetic domains phases, the vector microscopic magnetization mechanisms, including the domain walls motion and domains magnetization rotation.

$$[\Lambda] = \begin{bmatrix} \Lambda_{TD}(B_{TD}, B_{RD}, f) & \Lambda_{TRD}(B,\theta,f) \\ \Lambda^*_{TRD}(B,\theta,f) & \Lambda_{RD}(B_{TD}, B_{RD}, f) \end{bmatrix}_{(TD,RD)} \tag{12a}$$

$$\Lambda_{TRD}(B,\theta,f) = \Lambda'_{TRD}(B,\theta,f) + j\Lambda''_{TRD}(B,\theta,f) \tag{12b}$$

Both the electrical conductivity and the magnetic structure represented by $[\Lambda]$ are responsible for microscopic and macroscopic eddy currents and finally for the eddy current losses (classical and excess ones). The complete dynamic losses within time harmonics can be deduced from the magnetic field diffusion principles as explained in the following.

C. *Magnetic field diffusion*

1) *Diffusion-like equation*

Combining the Maxwell-Ampere and the Maxwell-Faraday equations and the behavioral model (1) in the (*TD,RD*) reference frame, one has to solve equation (13) by using the tensor $[\tau] = \sigma[\Lambda]^2[\mu_s]$, and by separating the static hysteresis contribution which does not involve any space variations related to the field diffusion effect.

$$-\frac{\partial^2}{\partial z^2}\left((1 + j\omega[\tau])\boldsymbol{H}_M\right) + j\omega\sigma[\mu_s]\boldsymbol{H}_M = 0 \tag{13a}$$

The solution of (13a) can be written in (13b) such that it provides the average flux density B as a function of the real $H'_{M,TD/RD}$ and imaginary $H''_{M,TD/RD}$ parts of the components *TD/RD* of vector $\boldsymbol{H}_M$ averaged through the sheet cross section:

$$\boldsymbol{B} = [\mu_s]\langle \boldsymbol{H}_M \rangle = \mu_0[\mu_{sr}]\begin{pmatrix} H'_{M,TD} + jH''_{M,TD} \\ H'_{M,RD} + jH''_{M,RD} \end{pmatrix}\frac{sinh(jk\zeta/2)}{jk\zeta/2} \tag{13b}$$

ζ is the sheet thickness and k is the wave vector obeying (13c)

$$det\begin{bmatrix} k^2(1 + j\omega\tau_{TD}) + j\omega\sigma\mu_{s,TD} & k^2 j\omega\tau_{TD-RD} + j\omega\sigma\mu_{s,TRD} \\ k^2 j\omega\tau_{RD-TD} + j\omega\sigma\mu_{s,TRD} & k^2(1 + j\omega\tau_{RD}) + j\omega\sigma\mu_{s,RD} \end{bmatrix} = 0 \tag{13c}$$

Then, the vector field $\langle \boldsymbol{H}_M \rangle$ with complex components in (*TD,RD*) can be calculated by solving the system given by (13d) with $(\alpha + j\beta) = (sinh(jk\zeta/2))/(jk\zeta/2)$, first with the flux density component B_{TD} ($B_{RD} = 0$) and then B_{RD} ($B_{TD} = 0$).

$$\begin{pmatrix} H'_{M,TD} \\ H''_{M,TD} \\ H'_{M,RD} \\ H''_{M,RD} \end{pmatrix} = \begin{bmatrix} +\alpha\mu_{s,TD} & -\beta\mu_{s,TD} & +\alpha\mu_{s,TRD} & -\beta\mu_{s,TRD} \\ -\beta\mu_{s,TD} & -\alpha\mu_{s,TD} & -\beta\mu_{s,TRD} & -\alpha\mu_{s,TRD} \\ +\alpha\mu_{s,TRD} & -\beta\mu_{s,TRD} & +\alpha\mu_{s,RD} & -\beta\mu_{s,RD} \\ -\beta\mu_{s,TRD} & -\alpha\mu_{s,TRD} & -\beta\mu_{s,RD} & -\alpha\mu_{s,RD} \end{bmatrix}^{-1}\begin{pmatrix} B_{TD} \\ 0 \\ B_{RD} \\ 0 \end{pmatrix} \tag{13d}$$

The magnetic field applied at the sheet surface in both (*TD,RD*) and (*x,y*) frames can then be calculated from (13e) and (13f)

$$\boldsymbol{H}_{a,(TD,RD)} = (1 + j\omega[\tau])\begin{pmatrix} H'_{M,TD} + jH''_{M,TD} \\ H'_{M,RD} + jH''_{M,RD} \end{pmatrix} cosh\left(\frac{jk\zeta}{2}\right) \tag{13e}$$

$$\boldsymbol{H}_{(x,y)} = [T]^{-1}\boldsymbol{H}_{(TD,RD)} \text{ and } \boldsymbol{B}_{(x,y)} = [T]^{-1}\boldsymbol{B}_{(TD,RD)} \tag{13f}$$

2) *Apparent magnitude permeability*

The apparent magnitude permeability, linked to each loop slope, defined as the ratio between the peak induction and the corresponding magnetic field on the loop, is given by (14a).

3) *Iron losses*

The dynamic iron losses, closely linked to each hysteresis loop area, is then given by the equation (14b).

$$\mu_{app,x\,/\,y}(B,\theta,f) = \frac{|B_{x/y}|}{|H_{x/y}(|B_{x/y}|)|} = \frac{module\left(\frac{B_{x\,or\,y}}{H_{x\,or\,y}}\right)}{\left|\cos\left(angle\left(\frac{B_{x\,or\,y}}{H_{x\,or\,y}}\right)\right)\right|} \tag{14a}$$

$$p_{dm}(B,f) = p_{fm}(B,f) - p_{hm}\frac{f}{5} = real\left(\frac{\boldsymbol{H}_a\cdot(j\omega\boldsymbol{B})^*}{2\gamma}\right) \tag{14b}$$

D. *Unknowns, working conditions – Identification strategy*

The two tensors $[\mu_{sr}]$ and $[\mu_{cr}]$ lead to 6 unknown components (3 each). The tensor $[\Lambda]$ contains 4 unknown components. The strategy proposed to identify the 10 unknowns in total.

1) *Quasi-static working conditions*

The identification procedure starts at low frequency to identify separately the components of static tensors: $[\mu_{sr}]$ and $[\mu_{cr}]$.

a) *Rolling and transverse directions*

Measurement of the permeability in both *RD* ($\mu_{app,x\,or\,y}(B,\theta = 90°\ or\ 0°, f = 5Hz)$) and *TD* ($\mu_{app,x\,or\,y}(B,\theta = 0°\ or\ 90°, f = 5Hz)$) for samples 0 and 90 (see Fig. 5 and TABLE 1) allows to identify the two diagonal components $\mu_{sr,TD}(B_{TD})$ and $\mu_{sr,RD}(B_{RD})$. Measurement of static hysteresis losses in the same directions ($P_{fh,x\,or\,y}(B,\theta = 90°\ or\ 0°)$ in *RD* and

$p_{hm,x\ or\ y}(B, \theta = 0°\ or\ 90°)$ in *TD*) for the same samples, allows to identify the diagonal components $\mu_{cr,TD}(B_{TD})$ and $\mu_{cr,RD}(B_{RD})$.

b) Misoriented flux with an angle θ

For misoriented fluxes forming an angle θ with *RD*, it can be shown that neither the magnitude permeability nor the static hysteresis losses in *y* or *x* directions can be accurately reproduced by using a simple combination of diagonal *TD* and *RD* properties and cosines and sines functions of θ. Thus, it is necessary to consider non diagonal properties inside any tensor $[\mu]$ and to use the frame change transfer rules as follows (15):

$$[\mu]_{(x,y)} = [T]^{-1}_{(TD,RD)-(x,y)}[\mu]_{(TD,RD)}[T]_{(TD,RD)-(x,y)} \quad (15)$$

Measurement of the permeability in any direction *x* or *y* ($\mu_{app,x\ or\ y}(B, \theta, 5Hz)$) for samples 15 to 75 (see Fig. 5 and TABLE 1) leads to the non-diagonal component $\mu_{sr,TRD}(B, \theta)$ of $[\mu_{sr}]$ as a function of *B* and θ. Measurement of static hysteresis losses in the same directions ($p_{hm,x\ or\ y}(B, \theta, 5Hz)$) for the same samples, allows to identify the non-diagonal component $\mu_{cr,TRD}(B, \theta)$ of $[\mu_{cr}]$ as a function of *B* and θ.

2) Dynamic working conditions

The next identification step include measurements at variable frequencies to identify separately the components of $[\Lambda]$.

a) Rolling and transverse directions

Simultaneous measurement of the dynamic permeability and losses in both the transverse direction ($\mu_{app,x\ or\ y}(B, \theta = 0°\ or\ 90°, f)\ and\ p_{dm}(B, \theta = 0°\ or\ 90°, f)$) and the rolling direction ($\mu_{app,x\ or\ y}(B, \theta = 90°\ or\ 0°, f)\ and\ p_{dm}(B, \theta = 90°\ or\ 0°, f)$) for samples numbered 0 and 90 (see Fig. 5 and TABLE 1) allows to identify the two diagonal components $\Lambda_{TD}(B_{TD}, B_{RD} = 0)$ and $\Lambda_{RD}(B_{TD}, B_{RD} = 0)$ of $[\mu_{sr}]$ first; then $\Lambda_{TD}(B_{TD} = 0, B_{RD})$ and $\Lambda_{RD}(B_{TD} = 0, B_{RD})$.

b) Misoriented flux with an angle θ

Simultaneous measurement of the angle and frequency dependent permeability and losses in both *x* and *y* directions ($\mu_{app,x\ and\ y}(B, \theta, f)\ and\ p_{dm}(B, \theta, f)$) for samples numbered from 15 to 75 (Fig. 5, TABLE 1) gives the real $\Lambda'_{TRD}(B, \theta, f)$ and imaginary $\Lambda''_{TRD}(B, \theta, f)$ parts of non-diagonal component $\Lambda_{TRD}(B, \theta, f)$ of $[\Lambda]$ as a function of *B*, θ and *f*.

E. Diagonalization conditions of Tensor properties

In case of diagonal tensors, the identification should lead to non diagonal components negligible compared to diagonal ones. The results in Fig. 9, Fig. 11, Fig. 17 and Fig. 18 reveal significant couplings between the *RD* and *TD* directions that appear for misoriented fluxes. The measurement data shows that the eigenvectors of the reference frame (***XH***,***YH***) able to diagonalize the tensor properties must be adapted to the variations of induction *B* and angle θ. The corresponding equivalent "hard" and easy" magnetic axis for each property can thus be revealed and valued by determining the eigenvectors and eigenvalues of $[\nu_s]$ and $[\nu_c]$.

III. Experiments – Permeability and Loss Measurements with Misoriented Flux

A. The experimental set-up

Magnetic measurements have been carried out with a Single Sheet Tester (SST150) adapted to 150*150 mm^2 specimens. Error is always under 5%: about 5% for $B \approx 0.1\ T$ and $f \approx 5\ Hz$, less than 1 % for $B \geq 1\ T$ and $f \geq 50\ Hz$. Error bars are not plotted on the upcoming figures for better legibility. Meanwhile, the SST magnetic circuit is closed and any demagnetizing effect due to the cutting angle should have a coefficient for such large samples below 1% of magnetization.

B. Material and samples

In order to characterize the 2D behavior with misoriented but 1-directional fields, seven GOES samples have been prepared with specific cutting angles (see Fig. 5 and TABLE 1).

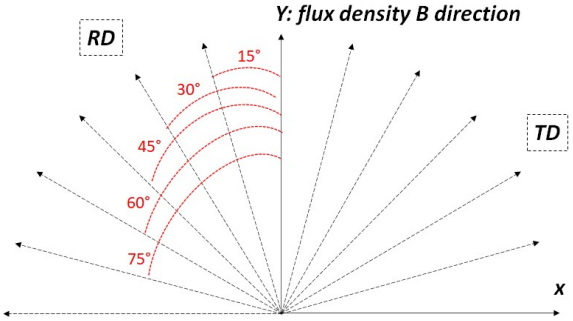

Fig. 5: Definition of cutting angles and flux density directions of specimens.

TABLE 1: LIST AND DESCRIPTION OF SAMPLES WITH CUTTING ANGLES

sample	Angle(*y*, *RD*) / Angle(***B***, *RD*)	Direction of flux ***B*** measured and components in (*TD*,*RD*) frame
0	*θ=0°/0°*	*y* ($B_{RD}=B_y$, $B_{TD}=B_x=0$)
0	*θ=0°/90°*	*x* ($B_{RD}=B_x=0$, $B_{TD}=B_y$)
15	*θ=15°/15°*	*y* ($B_{RD}=B_y cos15$, $B_{TD}= B_y sin15$)
15	*θ=15°/75°*	*x* ($B_{RD}=B_x cos75$, $B_{TD}= B_x sin75$)
30	*θ=30°/30°*	*y* ($B_{RD}=B_y cos30$, $B_{TD}= B_y sin30$)
30	*θ=30°/60°*	*x* ($B_{RD}=B_x cos60$, $B_{TD}= B_x sin60$)
45	*θ=45°/45°*	*y* ($B_{RD}=B_y cos45$, $B_{TD}= B_y sin45$)
45	*θ=45°/45°*	*x* ($B_{RD}=B_x cos45$, $B_{TD}= B_x sin45$)
60	*θ=60°/60°*	*y* ($B_{RD}=B_y cos60$, $B_{TD}= B_y sin60$)
60	*θ=60°/30°*	*x* ($B_{RD}=B_x cos30$, $B_{TD}= B_x sin30$)
75	*θ=75°/75°*	*y* ($B_{RD}=B_y cos75$, $B_{TD}= B_y sin75$)
75	*θ=75°/15°*	*x* ($B_{RD}=B_x cos15$, $B_{TD}= B_x sin15$)
90	*θ=90°/90°*	*y* ($B_{RD}=B_y cos90=0$, $B_{TD}=B_y sin90=B_y$)
90	*θ=90°/0°*	*x* ($B_{RD}=B_x cos0=B_x$, $B_{TD}=B_x sin0=0$)

C. *Quasi-static Measurements (f = 5Hz)*

1) *The B(H) curves and quasi-static permeability*

Fig. 6 shows the results on the apparent static magnetic permeability measured linking the magnitudes of H_y and B_y for the whole samples. As expected for GOES, the permeability for *y* parallel to *RD* is much higher than the permeability when *y* forms and angle θ with *RD*. Usually, the permeability is reduced when θ increases, however some marginal effects appear for weak and strong angles (θ<15° and θ>45°) (§ IV.A).

1) *The quasi-static hysteresis losses and coercive field*

Fig. 7 shows the results on the quasi-static hysteresis losses measured for the whole samples. As expected, the losses for *y* parallel to *RD* is much lower than the losses when *y* forms and angle θ with *RD*. [$\mu_c(B, \theta)$] variations are discussed in § IV.B.

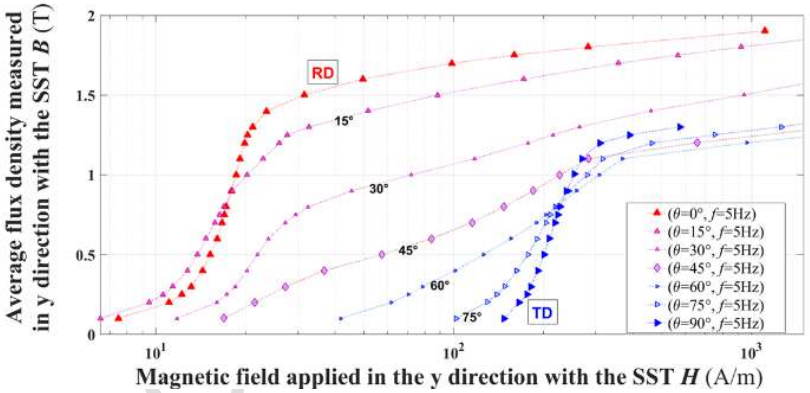

Fig. 6. *B(H)* curves measured on the seven samples at low frequency (*f=5Hz*) and as a function of the magnitude value of flux density *B* and its angle θ.

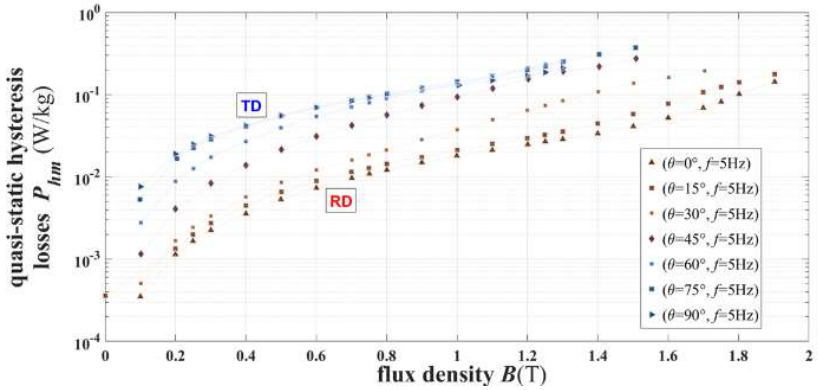

Fig. 7. Hysteresis losses $P_{hm}(B,\theta)$ measured on the 7 samples at low frequency (*f=5Hz*) as a function of the magnitude value of flux density *B* and its angle θ.

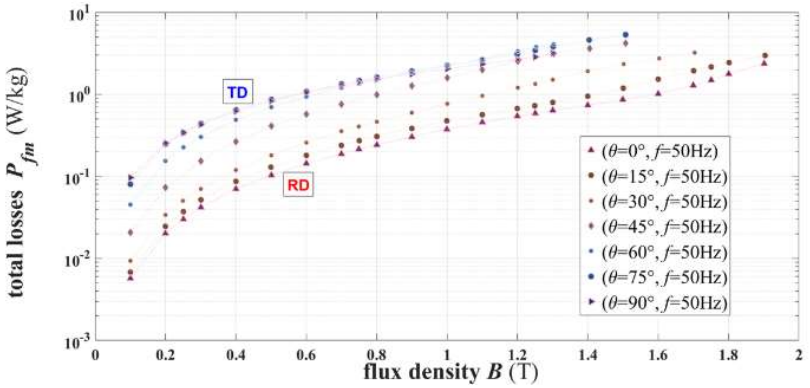

Fig. 8. Total losses $P_{fm}(B,\theta)$ measured on the 7 samples at frequency $f = 50$ *Hz* as a function of the magnitude value of flux density B and its angle θ.

D. Dynamic measurements (variable frequency, f = 50 Hz)

1) The Apparent Permeability $\mu_{app}(B,\theta,f)$

Dynamic $\mu_{app}(B,\theta,f)$ can be deduced from (14a) by using results similar to that of Fig. 6 with damping effects.

2) The dynamic losses $P_f(B,f)$

Fig. 8 shows the results on the total iron losses measured for the whole samples. As expected, the losses for $f >> 5$ *Hz* are mainly driven by the dynamic contributions. For *y* parallel to *RD* it is still much lower than the losses when *y* forms and angle θ with *RD*. $[\Lambda(B,\theta,f)]$ variations are discusses in § IV.A.

IV. Identifications – Tensor Magnetic Properties

A. Static internal permeability $[\mu_s(B,\theta)]$ *- discussions*

The identification procedure for each component of $[\mu_s(B,\theta)]$ is summed up with the equations (16) below:

$$\mu_{s,TD}(B_{TD}) = \mu_{app,y}(B, 90°, 5Hz) \tag{16a}$$

$$\mu_{s,RD}(B_{RD}) = \mu_{app,y}(B, 0°, 5Hz) \tag{16b}$$

$$\mu_{sr,TRD}(B,\theta) = \frac{\mu_{sr,TD}(B_{TD})\sin^2\theta + \mu_{sr,RD}(B_{RD})\cos^2\theta}{2\cos\theta\sin} - \mu_{app,y}(B,\theta,5Hz) \tag{16c}$$

Fig. 9 and Fig. 10 show the identifications of $[\mu_{sr}]$. At small angle θ, and for low or intermediate flux densities ($B<0.8T$), $\mu_{sr,TRD}$ can be negative even if lower than $\mu_{sr,RD}$, with beneficial impact on the *B(H)* curves corresponding to $\theta<15°$. The misoriented flux seems to activate a coupling between *TD* polarizations of domains with moving walls and *RD* components of main 180° domains. When θ is increased ($\theta\geq30°$, $B<0.8T$), $\mu_{sr,TRD}$ becomes positive with a negative impact on the *B(H)* curves with lower slopes. The higher the flux density ($B>0.8T$), the stronger the coupling term $\mu_{sr,TRD}$, comparable to $\mu_{sr,RD}$ or $\mu_{sr,TD}$. The maximum of $\mu_{sr,TRD}$ apparently always occur at the magnetization knee. For higher angles ($\theta\geq30°$, $B>0.8T$), $\mu_{sr,TRD}$ is decreasing with θ; however, for angles $\theta\geq45°$, $\mu_{sr,TRD}$ can still have a value bigger than $\mu_{sr,TD}$, such that the *B(H)* curves show a slope lower than in *TD*.
Fig. 13 and Fig. 14 show that while *B* increases, the "hard"/"easy" axis deviate from a direction close to *TD/RD* respectively (-15°<β<+15°) towards a direction forming a significant angle with *TD/RD* respectively (15°<β<40°).

B. The coercive permeability $[\mu_c(B,\theta)]$ *- discussions*

The identification procedure for each component of $[\mu_c(B,\theta)]$ is summed up with the equations (17) below:

$$\mu_{c,TD}(B_{TD}) = \frac{\pi f B_{TD}^2}{\gamma P_{fh}(B,\theta=90°,f=5Hz)} \tag{17a}$$

$$\mu_{c,RD}(B_{RD}) = \frac{\pi f B_{RD}^2}{\gamma P_{fh}(B,\theta=0°,f=5Hz)} \tag{17b}$$

$$\mu_{c,TRD}(B,\theta) = \frac{\mu_{c,TD}(B_{TD})\sin^2\theta + \mu_{c,RD}(B_{RD})\cos^2\theta}{2\cos\theta\sin\theta} - \frac{\pi f B^2}{\gamma P_{fh}(B,\theta f=5Hz)} \tag{17c}$$

Fig. 11 and Fig. 12 show the identifications of $[\mu_{cr}]$ similarly to $[\mu_{sr}]$. We notice a significant increase of $\mu_{cr,TRD}$ and hysteresis loss when $15°<\theta<45°$, which partly corresponds to the low values of $\mu_{cr,TRD}$ at its maximum compared to $\mu_{sr,TRD}$.
Fig. 15 and Fig. 16 show that while *B* increases, the "hard"/"easy" axis deviate from a direction close to *TD/RD* respectively (-10°<β<+10°) towards a direction forming a significant angle with *TD/RD* respectively (10°<β<30°).

A. The dynamic magnetization property $[\Lambda(B,\theta)]$

The identification procedure for each component of $[\Lambda(B,\theta)]$ is explained in § II.D.2) and with the equations in (13). In Fig. 17, Fig. 18 , Fig. 19 and Fig. 20, we notice the **N**ucleation/activation of specific domains with walls (**DWN**) and magnetization mechanisms at specific *B* values. Around 0.2 T: walls between new nucleated domains (Lancet and out-of-plane 45°-90° domains, Λ_{TD}) and source couplings between *TD* and *RD* (loss reduction, Λ'_{TRD}<0) start appearing with the **DWD** mechanism when magnetizing the sample with a significant *TD* component ($\theta \geq 45°$). Around 0.6 T: walls between previously nucleated domains start **F**using with lower density and mobility (**DWF**). The non-dissipative couplings between *TD* and *RD* (absorption of reactive power, Λ''_{TRD}) and the dissipative couplings (Λ'_{TRD}>0) start increasing when magnetizing in a direction forming an angle $30° < \theta < 45°$. Around 1 T: No more **DWD** and *RD* component of domains (Λ_{RD}) play any role when magnetizing the sample closer to *TD* ($\theta > 45°$). It is replaced by the **DMR** and Λ_{TD}. At 1.3 T and above: domains with *RD* components (Λ_{RD}) still play a role when magnetizing closer to *RD* ($\theta < 45°$) but the activated **DMR** mechanism with *TD* components becomes predominant (Λ_{TD}).

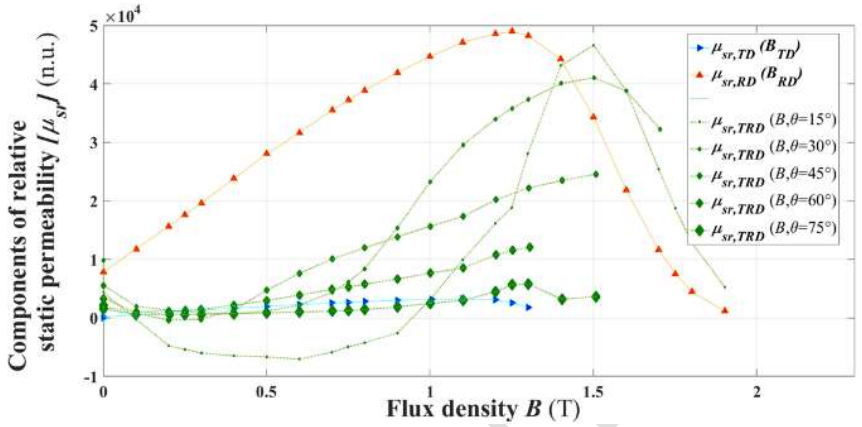

Fig. 9. Components of $[\mu_{sr}(B,\theta)]$ identified as a function of the magnitude value of flux density *B* for the whole angles θ(0°, 15°, 30°, 45°, 60°, 75°, 90°).

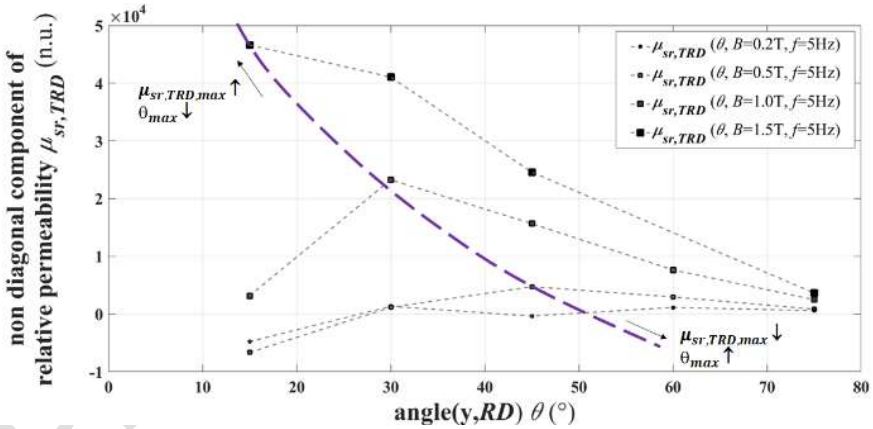

Fig. 10. Non diagonal component $\mu_{sr,TRD}(B,\theta)$ of $[\mu_{sr}]$ identified as a function of angle θ given the magnitude values of induction *B* (0.2 T, 0.5 T, 1 T, 1.5 T).

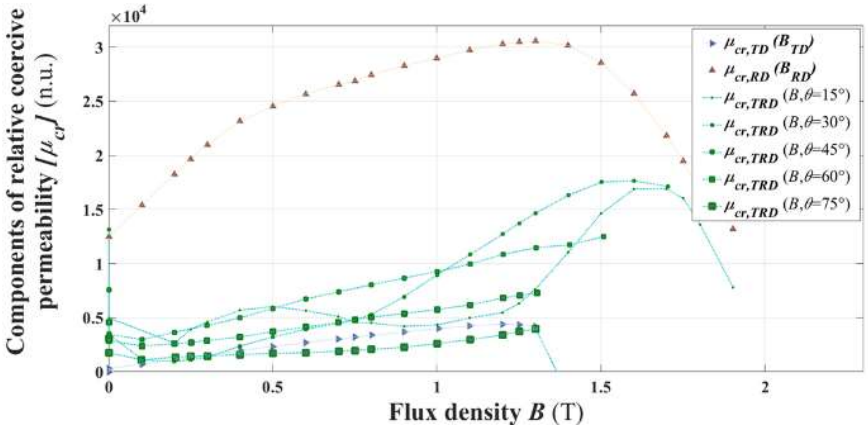

Fig. 11. Components of $[\mu_{cr}(B,\theta)]$ identified as a function of the magnitude value of flux density *B* for the whole angles θ(0°, 15°, 30°, 45°, 60°, 75°, 90°).

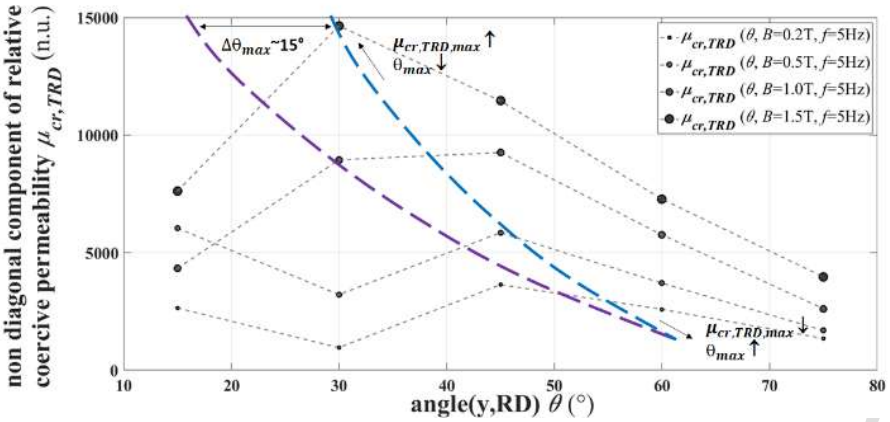

Fig. 12. Non diagonal component $\mu_{cr,TRD}(B,\theta)$ of $[\mu_{cr}]$ identified as a function of angle θ given magnitude values of induction B (0.2 T, 0.5 T, 1 T, 1.5 T).

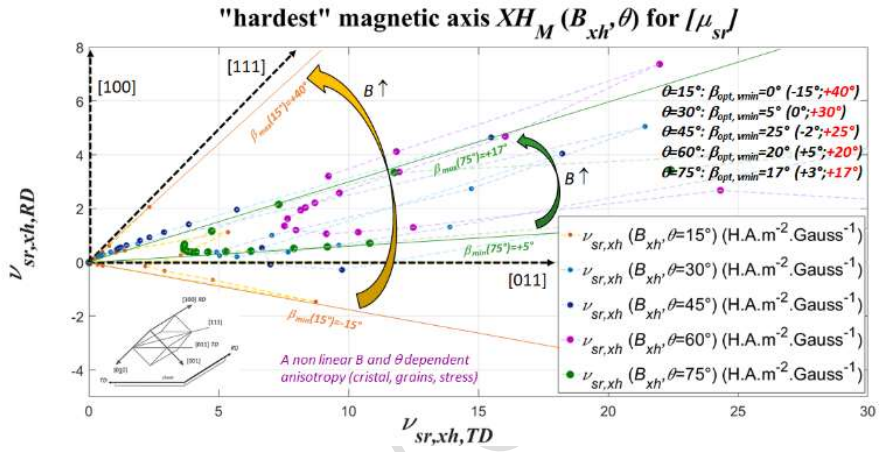

Fig. 13: eigenvectors $\boldsymbol{XH_M}$ and eigenvalues $\nu_{s,xh} = \nu_{sr,xh}\,\nu_0$ with the hardest quasi-static magnetization axis of tensor property $[\nu_s]$.

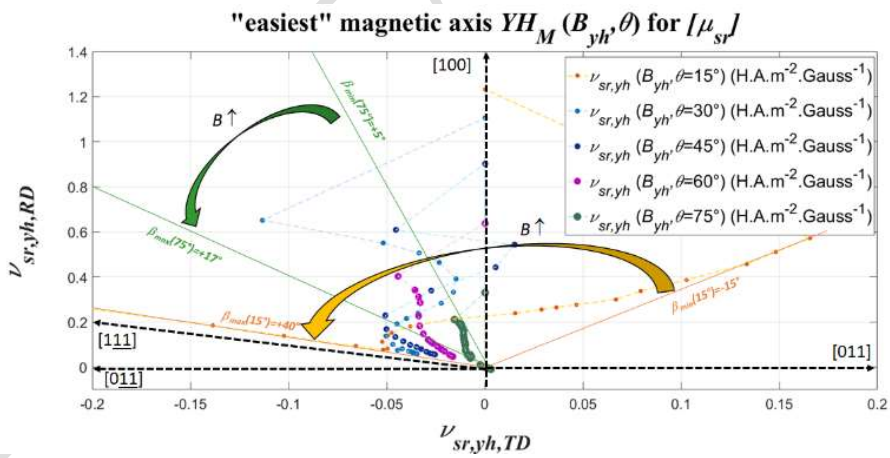

Fig. 14: eigenvectors $\boldsymbol{YH_M}$ and eigenvalues $\nu_{s,yh} = \nu_{sr,yh}\,\nu_0$ with the easiest quasi-static magnetization axis of tensor property $[\nu_s]$.

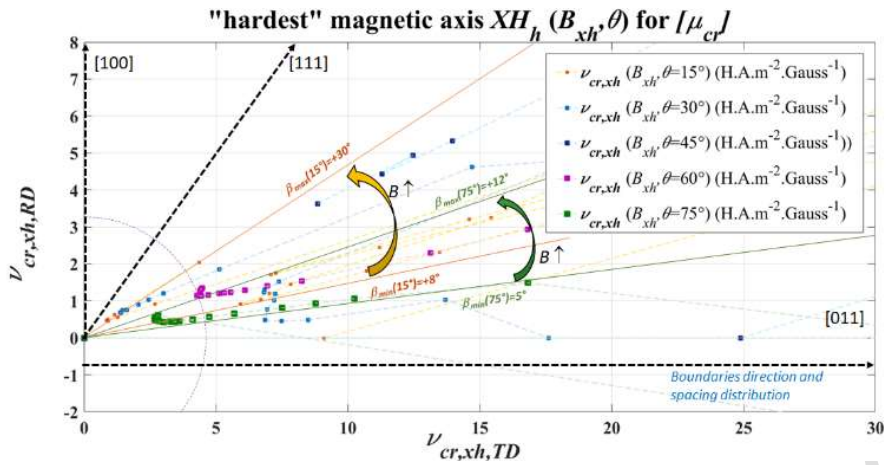

Fig. 15: eigenvectors $\boldsymbol{XH_h}$ and eigenvalues $\nu_{c,xh} = \nu_{cr,xh}\,\nu_0$ with the hardest static coercive field axis of tensor property $[\nu_c]$.

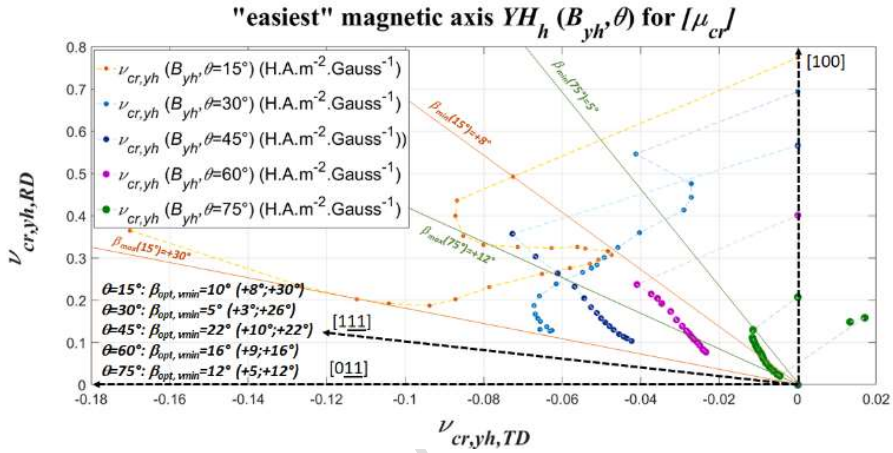

Fig. 16: eigenvectors $\boldsymbol{YH_h}$ and eigenvalues $\nu_{c,yh} = \nu_{cr,yh}\,\nu_0$ with the easiest static coercive field axis of tensor property $[\nu_c]$.

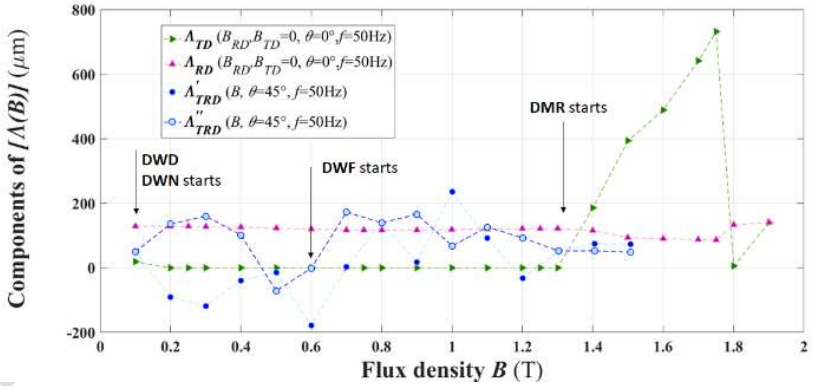

Fig. 17. Components of $[\Lambda(B,\theta)]$ identified at $f = 50\ Hz$ as a function of the magnitude value of flux density B for various angles θ(0°, 45°).

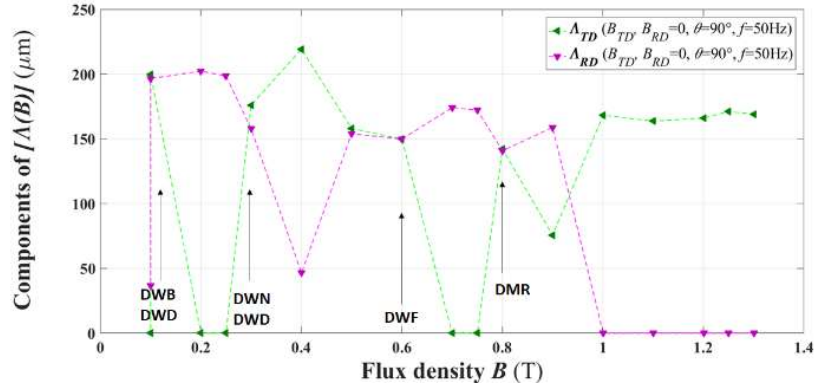

Fig. 18. Components of $[\Lambda(B,\theta)]$ identified at $f = 50\ Hz$ as a function of the magnitude value of flux density B for various angles θ(45°, 90°).

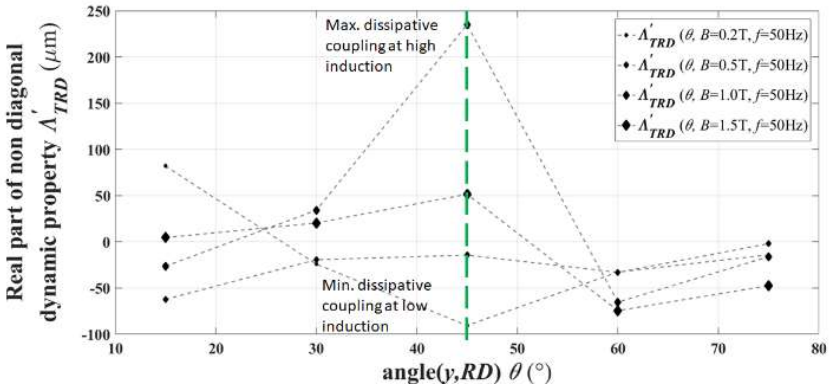

Fig. 19: Non-diagonal real component $\Lambda'_{TRD}(B,\theta,f)$ of $[\Lambda]$ identified at $f = 50$ *Hz* as a function of θ for various B (0.2 T, 0.5 T, 1 T, 1.3 T).

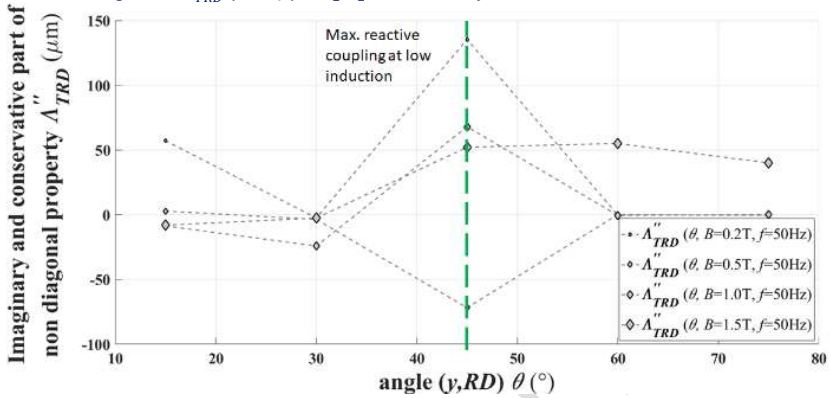

Fig. 20. Non-diagonal imaginary component $\Lambda''_{TRD}(B,\theta,f)$ of $[\Lambda]$ identified at $f = 50$ *Hz* as a function of θ for various B (0.2 T, 0.5 T, 1 T, 1.3 T).

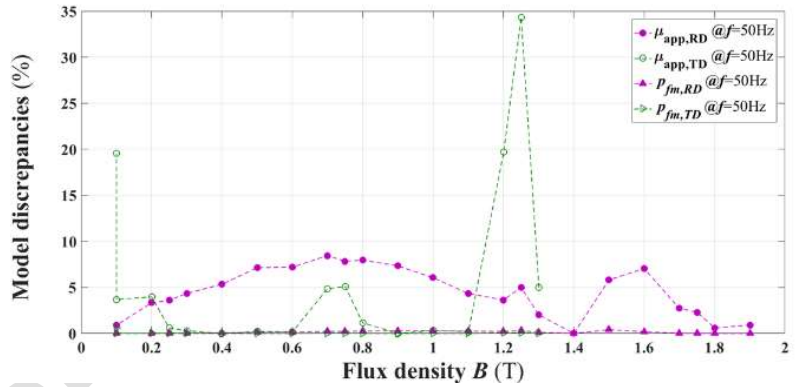

Fig. 21: Model discrepancies in both *TD* and *RD* directions for the estimation of permeability and losses @ f = 50 Hz as a function of B.

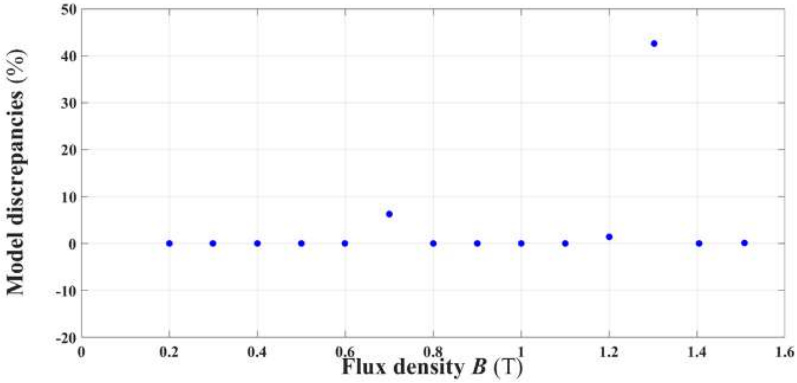

Fig. 22: Model discrepancies with misoriented flux (θ=45°) for the estimation of iron losses @ f = 50 Hz as a function of B.

V. Conclusion and Forthcoming

A mesoscopic tensor ***H(B)*** model dedicated to the description of the 2-D vectorial magnetic behavior and losses within quasi-static and magneto-harmonic working conditions is proposed. It is based on microscopic properties of magnetic domains and walls by separating the 2D vector magnetic field in three components. The latter involve tensor properties ($[\nu_s]$, $[\nu_c]$ and $[\Lambda]$) derived from physical energies. In the frequency domain, macroscopic eddy currents can be taken into account through the field diffusion-like equations. Analytical solutions of this 1-D problem within the sheet thickness but with in-plane fields in two directions are used to identify the magnetic properties by fitting the permeability or/and the losses measured. Identification are performed by magnetizing a GOES material at various angles θ between the flux and *RD*. It is shown that significant non linear non diagonal components of each tensor must be considered to include the couplings between *TD* and *RD*. The components of $[\Lambda]$ explain the role played by the magnetic domains, walls and the two main mechanisms **DWD** and **DMR** during a misoriented magnetization sequence. While *B* increases, the equivalent "hard"/"easy" axis for $[\nu_s]$ and $[\nu_c]$ deviate from a direction close to *TD/RD* towards a direction at 50°-70° from *RD/TD* which corresponds the 60° found in the literature. The methodology will be useful when investigating recrystallization processes or surface treatments. The same model could be used for NGOES. Experiments show that the role played by non diagonal components is less significant in NGOES than in GOES. The model fits well the iron losses in all directions but requires improvements to estimate better the permeability and predict hysteresis loops in each direction θ.

Acknowledgment

This work has received funding from the EC under the H2020-IND-CE-2016-17/H2020-FOF-2017 Prog. (Grant No. 766437).

References

[1] G.Bertotti, *J. of Mag. and Magnetic Materials*, vol. 41, 1984, p. 253-260.
[2] R.Pry & C.Bean, *J. of Applied Physics*, vol. 29, n° 3, 1958, p. 532-533.
[3] D.C. Jiles & D.L. Atherton, *J. Magn. Magn. Mater.,* Amsterdam, 1986.
[4] G. Bertotti, *IEEE Trans. on Mag*., vol. 24, no. 1, 1988, pp. 621-630
[5] D.-X.Chen et al., *IEEE Trans. on Mag.*, vol. 33, n° 3, 1997, p. 2229-2244.
[6] M. Enokizono, *J. of Mat. Proc. Tech.,* vol. 108, no. 2, 2001, pp. 231-255.
[7] M.-A. Raulet et al., *IEEE Trans. on Mag.*, vol. 42, n°2, 2004, p. 872-875.
[8] O. Maloberti et al., *la RIGE*, conférence MGE, Lyon, 2005.
[9] C. Appino et al., *J. of Mag. and Mag. Mat.,* vol. 500, 2020, pp. 166-281.